JACS
JOURNAL OF THE AMERICAN CHEMICAL SOCIETY
pubs.acs.org/JACS
Article

Fluoride- and Seed-Free Synthesis of Pure-Silica Zeolite Adsorbent and Matrix Using OSDA-Mismatch Approach

Chao Ma, Xiaona Liu, Yang Hong, Nana Yan, Chenyang Nie, Jing Wang, Peng Guo,* and Zhongmin Liu*

Cite This: J. Am. Chem. Soc. 2023, 145, 24191−24201
Read Online
ACCESS | Metrics & More | Article Recommendations | Supporting Information

ABSTRACT: The pure-silica zeolite plays a crucially important role in the gas separation of alkane/alkene, the low-k dielectric material, and the robust matrix for confining metal species during catalysis. However, the environmentally friendly synthesis of pure-silica zeolites is still challenging since (1) the toxic fluoride or dealuminum seeds are inevitably utilized through the hydrothermal synthesis and (2) it will also take a longer crystallization time. Herein, we present an efficient method called the OSDA-mismatch approach for the fluoride- and seed-free synthesis of pure-silica zeolites using **Si-SOD** (enriched 4-rings) as the sole silica source. This approach allows for the rapid and green synthesis of 15 pure-silica zeolites (**CHA**, ***BEA**, **EUO**, **SFF**, **STF**, **-SVR**, ***-SVY**, **DOH**, **MTN**, **NON**, ***MRE**, **MEL**, **MFI**, **MTW**, and ***STO**). Furthermore, distinct crystallization mechanisms of two significant pure-silica **CHA**- and ***BEA**-type zeolites (denoted as **Si-CHA** and **Si-BEA**) are investigated in detail by advanced characterization techniques such as FIB, 3D ED, 4D-STEM, HRTEM, Raman, and ^{29}Si MAS NMR. More importantly, **Si-CHA** displays promising propane/propylene separation performance even better than the one synthesized in the presence of toxic HF. In addition, the incorporation of Zn species within **Si-BEA** fabricated by this approach also renders superior performance on propane dehydrogenation.

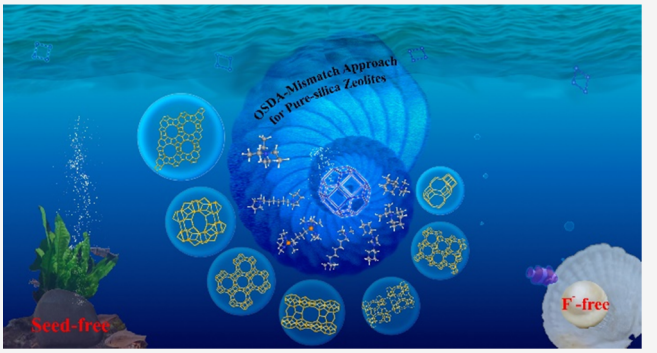

INTRODUCTION

Pure-silica zeolites, which contain well-defined channel systems and/or cavities with molecular-sized pore openings constructed by the conner-sharing SiO_4, have garnered increasing scientific and industrial attention. It is due to their wide applications as matrixes confining metal species for further catalysis, low-k dielectric materials, and adsorbents for separating alkane/alkene, etc.[1−8] Currently, there are 260 framework-type codes (FTCs) approved by the International Zeolite Association-Structure Commission (IZA-SC), while only 58 FTCs can be available in pure-silica forms.[9−11] Unfortunately, in most cases, pure-silica zeolites can be synthesized only in the presence of toxic fluoride by conventional hydrothermal synthesis, hindering their further industrial applications. Thus, many efforts have been devoted to synthesizing pure-silica zeolites in the absence of fluorides. One of the synthetic strategies for overcoming this challenge is the utilization of pure-silica seeds combined with inorganic cations,[12−14] the pore filling ethanol, and other pure-silica zeolite as the main silica resource,[15,16] respectively. Unfortunately, such pure-silica seeds are inevitably synthesized in the fluoride medium or processed by dealumination postsynthesis. Another strategy is the dry-gel conversion, which allows for fluoride- and seed-free synthesis of a series of pure-silica zeolites.[17] However, this approach typically requires a longer crystallization time. Recently, a microwave-assisted hydrothermal strategy has been developed for fluoride- and seed-free synthesis of pure-silica ***BEA** zeolite with the assistance of L-lysine in a concentrated gel system.[18] For commercial viability, it is desirable to develop easy-to-use fluoride- and seed-free synthesis approaches that are expected to be applicable to a broad range of zeolite topologies, improving the overall efficiency of synthesis and reducing costly reagents.

Before a new synthetic methodology is developed, the roles of fluorine ions should be understood and summarized. First, it can accelerate the polymerization and hydrolysis of silicate species.[19] Second, negative charges of fluorine ions can balance positive charges from organic structure-directing agents (OSDAs) in the final crystalline pure-silica zeolites.[20] Without fluorine ions, defects in the framework balancing positive charges from the OSDA inevitably emerge. Third, fluorine ions

Received: August 4, 2023
Revised: October 7, 2023
Accepted: October 11, 2023
Published: October 25, 2023

https://doi.org/10.1021/jacs.3c08484
J. Am. Chem. Soc. 2023, 145, 24191−24201

can stabilize the specific composite building units (CBUs) rich in 4-rings such as *d4r* (4^6), *bea* ($4^3 5^2 6^1$), and *rth* ($4^4 5^4$).[21] It seems if appropriate pure-silica zeolites rich in 4-rings are chosen as the sole source, it may facilitate the fluoride-free synthesis of pure-silica zeolites in the absence of corresponding seeds through the interzeolite conversion. In this case, how to choose a suitable OSDA becomes a significant issue; otherwise, the selected OSDA will not direct the targeted product but promote the recrystallization of parent pure-silica zeolites. Therefore, the key to developing the new green synthetic methodology is to identify the mismatch nature between selected OSDAs and parent pure-silica zeolites.

Herein, we present a general and efficient method, called the OSDA-mismatch approach, for fluoride- and seed-free synthesis of pure-silica zeolites with distinct topologies in a short crystallization time. In this work, nonporous **SOD**-type pure-silica zeolite (denoted as **Si-SOD**) containing smaller *sod* cages are judiciously selected as the sole silica source since they are rich in 4-rings and can be easily inhibited by utilizing larger OSDA in size. In this case, a series of pure-silica zeolites with **CHA**, ***BEA**, **EUO**, **SFF**, **STF**, **-SVR**, ***-SVY**, **DOH**, **MTN**, **NON**, ***MRE**, **MEL**, **MFI**, **MTW**, and ***STO** topologies are rapidly synthesized under fluoride-free conditions, even without any seeding assistance. Moreover, the distinct crystallization pathways of two important **CHA**- and ***BEA**-type pure-silica zeolites (denoted as **Si-CHA** and **Si-BEA**) are well investigated by advanced characterization techniques such as focusing ion beam (FIB), three-dimensional electron diffraction (3D ED), four-dimensional scanning transmission electron microscopy (4D-STEM), high-resolution transmission electron microscopy (HRTEM), Raman, and ^{29}Si MAS NMR. We not only illustrate the potential wide applicability of this OSDA-mismatch method but also demonstrate that **Si-CHA** and **Si-BEA** prepared through this approach exhibit propylene/propane adsorptive separation and serve as matrixes confining metal species for propane dehydrogenation, respectively.

RESULTS AND DISCUSSION

Synthesis of Pure-Silica Zeolites by OSDA-Mismatch Approach. As previously mentioned in the Introduction section, nonporous **SOD**-type pure-silica zeolites can be chosen as the exclusive silica source for several reasons. First, they can be synthesized without the need for fluorides, simplifying the production process. Second, they contain a high proportion of 4-rings, which can potentially enhance the crystallization rate of the desired products. Lastly, this topology is composed solely of smaller *sod* cages, and by utilizing larger OSDAs, its recrystallization process can be effectively inhibited. The inherent mismatch between the parent zeolites, serving as the exclusive silica source, and the OSDAs employed can be readily recognized, leading to the successful synthesis of the desired zeolites via interzeolite transformation. Therefore, we called this method the OSDA-mismatch approach (Figure 1).

In this case, the **Si-SOD** parent zeolites were conveniently prepared through a straightforward process involving the grinding of solid silica and ethylene glycol, followed by crystallization (details in the Experimental Section). Additionally, we examined the impact of utilizing the smaller classical OSDA, tetramethylammonium hydroxide (TMAOH in Figure S1), in conjunction with **Si-SOD** as the exclusive silica source. Notably, it resulted in the recrystallization of **Si-SOD**, as depicted in Figure S2. Subsequently, utilizing a series of larger OSDAs (Figure S1) and **Si-SOD**, 15 pure-silica zeolites (**CHA**, ***BEA**, **EUO**, **SFF**, **STF**, **-SVR**, ***-SVY**, **DOH**, **MTN**, **NON**, ***MRE**, **MEL**, **MFI**, **MTW**, and ***STO**) as shown in Table 1 were simply and rapidly synthesized in the fluoride- and seed-free condition. These can be categorized into two groups:

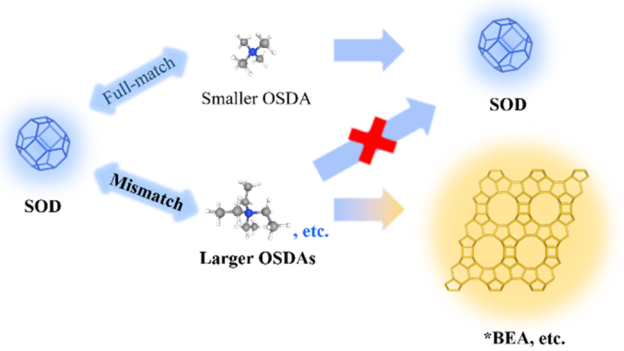

Figure 1. Schematic representation of the proposed OSDA-mismatch approach.

(1) It is important to highlight that seven pure-silica zeolites (**CHA**, ***BEA**, **EUO**, **SFF**, **STF**, **-SVR**, and ***-SVY**), traditionally requiring hydrothermal synthesis in a fluoride medium, can be successfully obtained using the OSDA-mismatch approach without the need for fluorides or seeds (Group I in Table 1). Moreover, **CHA**-, ***BEA**-, **EUO**-, **SFF**- and ***SVY**-type pure-silica zeolites can maintain their crystallinities after removing OSDAs within channels or cavities, verified by BET results and PXRD patterns (Figures S3−S8 and Table S1).

(2) In further, this approach is further extended to accelerate the preparation of other pure-silica zeolites with **DOH**, **MTN**, **NON**, ***MRE**, **MEL**, **MFI**, **MTW**, and ***STO** structures, which can be hydrothermally synthesized in the alkaline medium. This strategy not only achieves the fluoride- and seed-free synthesis of pure-silica zeolites but also effectively reduces their crystallization time (Group II in Table 1). Detailed descriptions of the high crystallinity and product yield of all synthesized pure-silica zeolites are provided in the Supporting Information (Figures S9−S16 and Table S2).

Among this series of synthesized pure-silica zeolites through the OSDA-mismatch approach, we select crucially important pure-silica zeolites **Si-CHA** and **Si-BEA** as examples for detailed investigations. Interestingly, partial substitution of **Si-SOD** with conventional silica sources can still lead to the synthesis of **Si-CHA** and **Si-BEA** as primary products (Tables S3−S4 and Figures S17−S18). In this study, we continue to emphasize **Si-SOD** as the exclusive silica source for subsequent synthesis investigations.

Crystallization Process of Si-CHA through OSDA-Mismatch Approach. The **Si-CHA** zeolite crystallized within 48 h by utilizing the conventional OSDA *N*,*N*,*N*-trimethyl-1-adamantammonium hydroxide (TMAdaOH), which can efficiently inhibit the recrystallization of **Si-SOD**. SEM images show that the final **Si-CHA** zeolite has well-defined morphology and grows in aggregates (Figure 2a). PXRD, BET area (621.74 $m^2 g^{-1}$), and micropore volume (0.326 $cm^3 g^{-1}$) confirm its high crystallinity after direct calcination

https://doi.org/10.1021/jacs.3c08484
J. Am. Chem. Soc. 2023, 145, 24191−24201

Table 1. Information on 15 Pure-Silica Zeolites Rapidly Synthesized in the Fluoride- and Seed-Free Condition with the OSDA-Mismatch Approach

				gel composition				
	FTCs	ring sizes	CBUs	OSDA[b]	$OSDA/SiO_2$[c]	H_2O/SiO_2	T (°C)/time (days)	reference time (media)
I[a]	***BEA**	4, 5, 6, 12	*mor, bea, mtw*	TEAOH	0.45	6	150/2.3	3 days (F^-)
	CHA	4, 6, 8	*d6r, cha*	TMAdaOH	0.2	15	150/2	5 days (F^-)
	EUO	4, 5, 6, 10	*non, cas*	$HM(OH)_2$	0.15	7	175/4	15 days (F^-)
	SFF	4, 5, 6, 10	*stf, cas*	DEDMPOH	0.2	7	150/2	7 days (F^-)
	STF	4, 5, 6, 10	*stf, cas*	$1,4\text{-TDEAP}(OH)_2$	0.2	10	175/4	14 days (F^-)
	-SVR	4, 5, 6, 10	*mor, mfi*	$1,6\text{-MPH}(OH)_2$	0.1	7	150/5	22 days (F^-)
	***-SVY**	4, 5, 6, 10, 14	*d6r, mel*	1,3-Dcyh-MIOH	0.2	7	150/5	8 days (F^-)
II[a]	**DOH**	4, 5, 6	*mtn, doh*	1,2,2,6,6-PMePDOH	0.2	10	150/4	46 days (OH^-)
	MTN	5, 6	*mtn*	BnTMAOH	0.2	7	150/5	7 days (OH^-)
	NON	4, 5, 6	*non*	$1,4\text{-MPB}(OH)_2$	0.2	10	175/5	15 days (OH^-)
	***MRE**	4, 5, 6, 10	*afi, mel, imf*	$HM\text{-C4}(OH)_2$	0.15	10	175/2	2 days (OH^-)
	MEL	4, 5, 6, 8, 10	*mor, mel, mfi*	TBAOH	0.25	20	160/2	4 days (OH^-)
	MFI	4, 5, 6, 10	*mor, cas, mfi, mel*	TPAOH	0.2	7	175/0.25	1 days (OH^-)
	MTW	4, 5, 6, 12	*jbw, cas, bik, mtw*	1,1-DM-4-cyhPZOH	0.2	7	150/5	12 days (OH^-)
	***STO**	4, 5, 6, 12	*ats, afs, bog, mel, imf, doh, dcc, nsc*	1,2,3-TE-4M-MIOH	0.2	7	150/7	10 days (OH^-)

[a]Group I comprises several pure-silica zeolites that are typically synthesized hydrothermally in the fluoride media, as reported in the literature.[7,23−28] Group II contains pure-silica zeolites that can be hydrothermally synthesized in the alkaline media.[29−36] [b]Abbreviations of OSDAs utilized in this study, along with their corresponding structural formulas, can be found in the Supporting Information. [c]**Si-SOD** is used as the sole silica source.

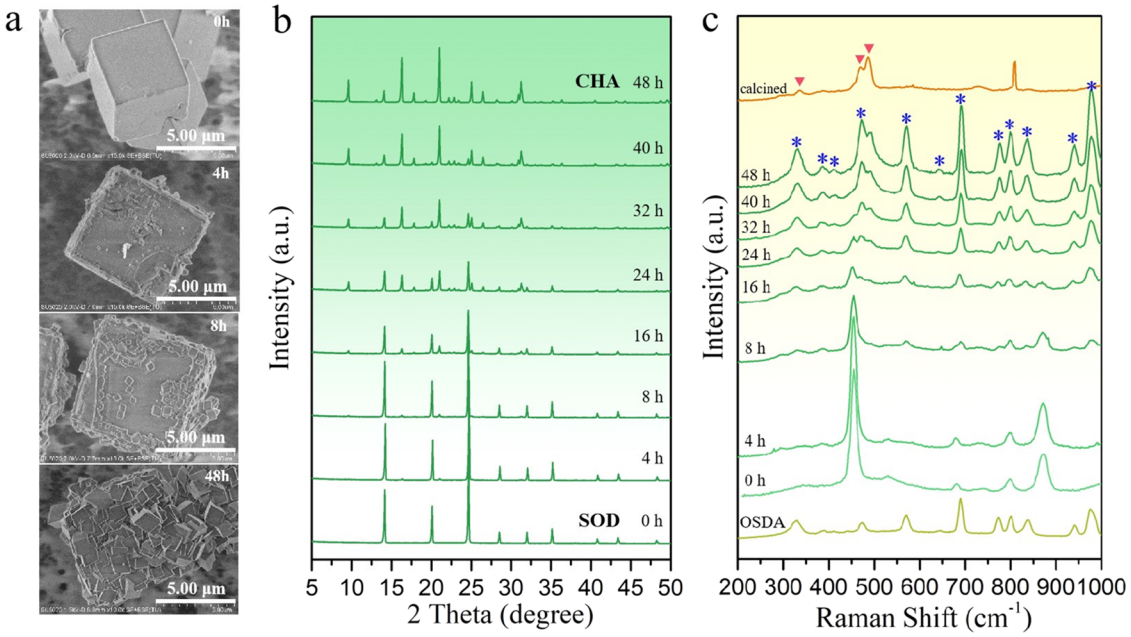

Figure 2. (a) SEM images of **Si-CHA** crystallized for 0, 4, 8, and 48 h. (b) PXRD patterns of **Si-CHA** with different crystallization times (0, 4, 8, 16, 24, 32, 40, and 48 h) from the bottom to the top. (c) Raman spectra of solid sample for **Si-CHA** during the crystallization process. The bands marked with blue stars correspond to the vibrations of the OSDAs, which exhibit consistency with the Raman spectra of the OSDA in the aqueous phase. The bands marked with red triangles are indicative of vibrations associated with the **CHA** framework.

(Figure S3 and Table S1). ^{13}C MAS NMR spectrum shows that OSDAs remain intact in the as-made sample (Figure S19). The ^{29}Si MAS NMR spectrum of the as-made sample shows peaks at −100.40 and −110.20 ppm, which belong to Q^3 and Q^4 species,[17] respectively (Figure S20). As illustrated in the ^{29}Si MAS NMR spectrum, although Q^3 species (silanol groups) also exist in the calcined sample, their content decreases to 9.60% (Figure S20 and Table S5). The peak at 3734 cm^{-1} in the IR spectrum of the calcined sample is assigned to silanol groups (Figure S21),[22] which is consistent with the result of ^{29}Si MAS NMR.

More importantly, we also study the crystallization process, interzeolite transformation from **Si-SOD** to **Si-CHA**. As shown in Figure 2b, the PXRD pattern shows that the obtained sample before hydrothermal treatment (0 h) is the parent **Si-SOD** material. The SEM image shows that smooth surfaces of the parent **Si-SOD** material are slightly dissolved and the overall morphology (8 um) remains integrated (Figures 2a and

https://doi.org/10.1021/jacs.3c08484
J. Am. Chem. Soc. 2023, 145, 24191−24201

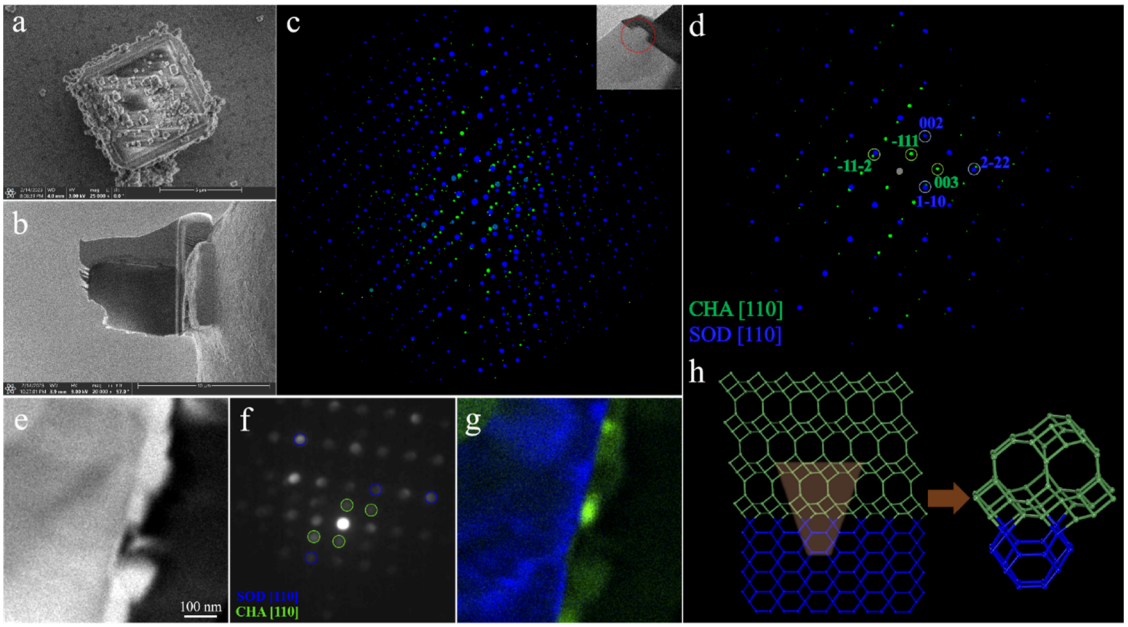

Figure 3. (a) SEM image of selected **SOD**-to-**CHA** grain for the FIB processing. (b) Cross-sectional specimen prepared and thinned to a thickness of 100 nm. (c) Reconstructed 3D ED of heterojunction section of **SOD**-to-**CHA** from the cRED data. The red circle area in the inset TEM image was used for cRED data collection. (d) Reciprocal plane cut from 3D ED. Virtual imaging in 4D-STEM: (e) overall real space; (f) reciprocal space; (g) virtual image generated from regions of interest. (h) Fully connected structural model of **SOD**-to-**CHA** intergrowth section.

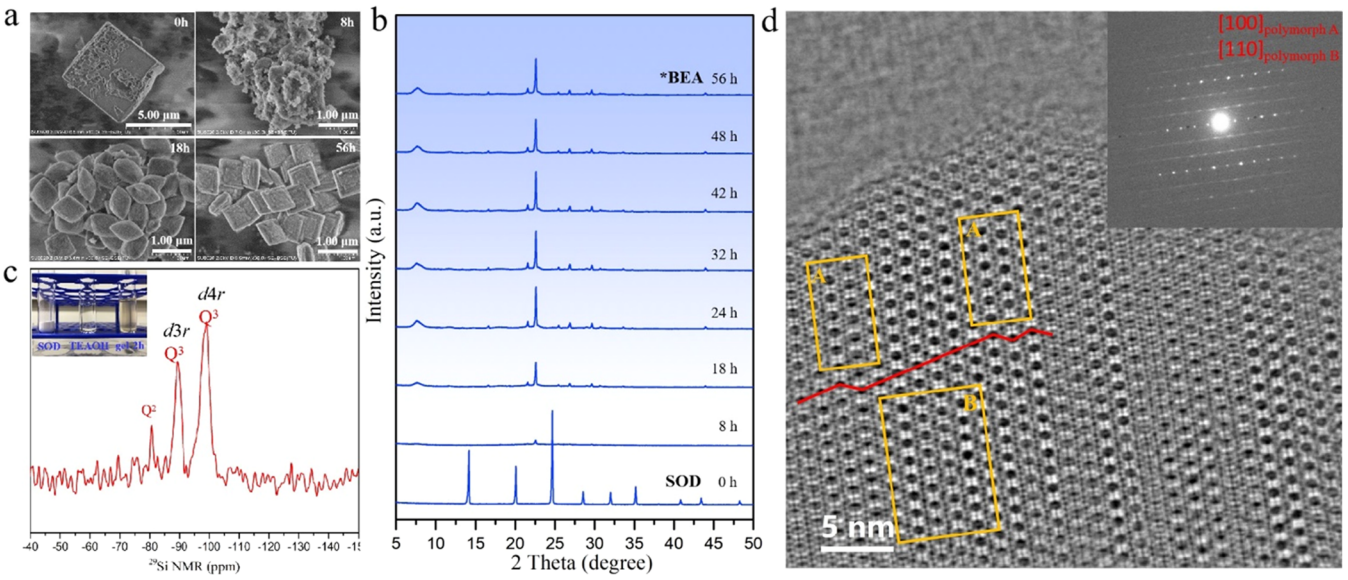

Figure 4. (a) SEM images of **Si-BEA** crystallized for 0, 8, 18, and 56 h. (b) PXRD patterns of **Si-BEA** with different crystallization times (0, 8, 18, 24, 32, 42, 48, and 56 h) from the bottom to the top. (c) Liquid ^{29}Si NMR spectrum of clear precursor solution for **Si-BEA** crystallized for 2 h. (d) iDPC-STEM image of **Si-BEA** taken along the direction of 12-ring channels. The pore stacking is marked. The inset picture is the corresponding SAED pattern with streaks perpendicular to the building layers.

S22). After 4 h of heating, the **Si-SOD** surface becomes rough, and a small number of **Si-CHA** particles (200−300 nm) with no distinct morphology attach on the **Si-SOD** substrate. Diffraction peaks belonging to the **Si-CHA** phase start to emerge along with the **Si-SOD** phase (Figure 2b). When crystallized for 8 h, more **Si-CHA** particles with larger size (500 nm) emerge. Extending the crystallization time (16−48 h), **Si-CHA** particles continue to grow and finally completely cover the parent **Si-SOD** material (Figure 2a). The PXRD patterns also exhibit that the **Si-CHA** phase increases while the **Si-SOD** phase decreases (Figure 2b). Current results revealed by SEM and PXRD indicate that **Si-CHA** were synthesized through the heteroepitaxial growth on the surface of **Si-SOD.** Moreover, we also observe that 4-rings (456 cm^{-1}) belonging to **Si-SOD** transform to 4-rings (486 and 470 cm^{-1}) of **Si-CHA** using Raman spectrum (Figure 2c).[37]

In order to further understand the origin of heteroepitaxial growth from **Si-SOD** to **Si-CHA** at the atomic level, a sample crystallized 8 h is selected to process by advanced FIB (Figure 3a). The cross-sectional specimens were prepared along the face diagonal direction of **Si-SOD** and thinned down to 100 (Figure 3b) and 50 nm by a gallium ion beam (Figure S23a),

https://doi.org/10.1021/jacs.3c08484
J. Am. Chem. Soc. 2023, 145, 24191−24201

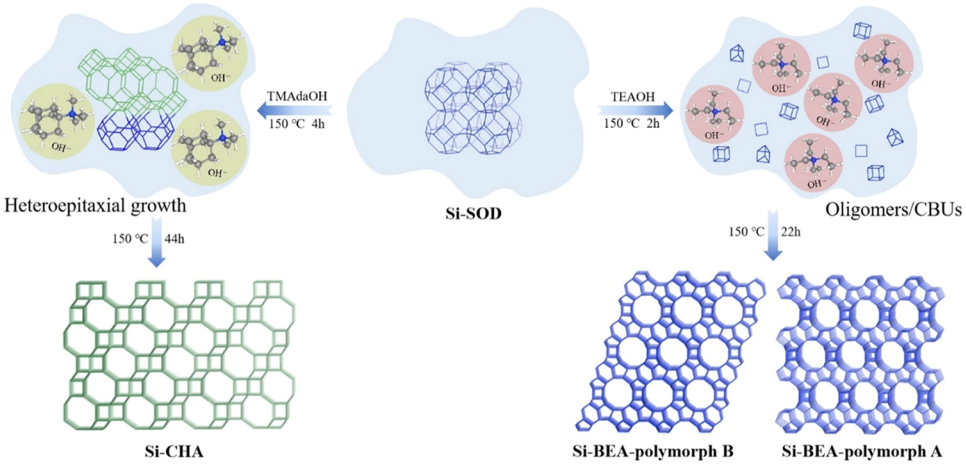

Figure 5. Schematic representation of the proposed crystallization pathways for **Si-CHA** and **Si-BEA** zeolites from parent **Si-SOD** zeolite in fluoride- and seed-free conditions with OSDA-mismatch approach.

respectively. Heterojunction section of the **SOD-to-CHA** specimen sample with 100 nm thickness was used to collect cRED data. The reconstructed 3D ED shows that two sets of ED from **Si-SOD** and **Si-CHA** coexist as shown in Figure 3c. It is worth noting that the reciprocal plane cut from 3D ED illustrates that reflection 002 from the **Si-SOD** substrate overlaps reflection −222 from **Si-CHA** (Figure 3d), which indicates that (002) crystallographic planes of **Si-SOD** align with (−222) planes of **Si-CHA.** 4D-STEM result of the specimen sample with 100 nm thickness further shows the defined regions of **Si-SOD** (marked blue) and **Si-CHA** (marked green) phases clearly (Figure 3e−g). The specimen sample with 50 nm thickness was used to investigate the **SOD-to-CHA** intergrowth section through the low-dose HRTEM imaging technique (Figure S23a−f). The relative orientation between **Si-SOD** and **Si-CHA** can also be deduced from Fast Fourier Transform (FFT) analysis of HRTEM images taken along the [110] zone axis of both samples, which are consistent with the 3D ED data (Figure S23g−h). More importantly, *d6r* as the terminal CBUs in **Si-CHA** can be clearly observed (Figure S23e). Based on the provided structural information, a series of structural models were constructed to uncover the atomic structure of the **SOD-to-CHA** heterojunction (Figures 3h and S24). If only fully connected structural models are considered, then Figure 3h displays the atomic structure at the interface. It illustrates that the terminated 4-rings of **Si-SOD** were directly connected to the 4-rings of **Si-CHA**.

Crystallization Process of Si-BEA through OSDA-Mismatch Approach. Utilizing the OSDA-mismatch approach, the **Si-BEA** zeolite has also been successfully synthesized within 56 h in the absence of fluorides and any seed. The conventional OSDA, tetraethylammonium hydroxide (TEAOH), was employed in the recipe, which cannot fit into the smaller *sod* cages of the parent **Si-SOD** and effectively suppresses its recrystallization. The final **Si-BEA** zeolite shows the square blocks morphology with the rough surface (Figure 4a). The PXRD results of the calcined **Si-BEA** sample show its high crystallinity. BET area and micropore volume are 590.59 $m^2\ g^{-1}$ and 0.261 $cm^3\ g^{-1}$, respectively (Figure S3 and Table S1). ^{13}C MAS NMR spectrum shows OSDAs maintain intact in the as-made sample (Figure S19). **Si-BEA** also have silanol groups (3705 cm^{-1} in IR spectrum)[22] and the content of Q^3 species (−101.10 ppm in ^{29}Si MAS NMR spectrum)[17] decreases to 7.88% after removing OSDAs (Figures S20−S21 and Table S5).

Compared with the heteroepitaxial growth mechanism unraveled in the **Si-CHA** system, that of **Si-BEA** is quite distinct. Although the sample obtained before heating (0 h) also shows characteristic peaks of the parent **Si-SOD** material, their surface is partially dissolved (Figure 4a−b). After heating for 2 h, the parent **Si-SOD** is completely dissolved forming a clear solution (Figure 4c). In order to obtain valuable information of siliceous species, which is crucial for deducing the crystallization mechanism, we investigate this clear solution using ^{29}Si NMR. It shows this clear solution has some double 3-rings (−89.40 ppm) and *d4r*s (−99.10 ppm) siliceous species (Figure 4c and Table S6).[38−41] Extending the crystallization time to 8 h, along with lots of amorphous particles start to appear (verified by PXRD pattern and SEM image). Subsequently, there is a decrease in the number of amorphous particles, followed by an increase in the **Si-BEA** phase, and ultimately the formation of uniformly sized **Si-BEA** particles with a diameter of 500 nm after 18 h of heating (Figure 4a). By extending the crystallization time to 56 h, there is an improvement in their crystallinity, accompanied by slight changes in their morphologies (Figures 4a−b and S25). Polymorph A, polymorph B, and their stacking sequence in **Si-BEA** are clearly observed in the integrated differential phase-contrast scanning transmission electron microscopy image (Figure 4d).

Based on the systemic structural investigations, we propose the following possible crystallization pathways for **Si-CHA** and **Si-BEA** (Figure 5). In the case of **Si-CHA**, (i) a small amount of parent **Si-SOD** zeolites dissolve and **Si-CHA** zeolites grow heteroepitaxially on its surface. (ii) Parent **Si-SOD** zeolites gradually dissolve and transform to **Si-CHA** zeolite completely. In the **Si-BEA** situation: (i) Parent **Si-SOD** zeolites first dissolve completely, forming the clear solution. (ii) **Si-BEA** along with amorphous particles emerge. (iii) Amorphous particles are further consumed completely and the highly crystalline **Si-BEA** forms.

The primary cause of these differences is attributed to the variance in alkalinity supplied by OSDA in the synthesized gels. In the gel composition for **Si-CHA**, the $TMAdaOH/SiO_2$ molar ratio is 0.2, indicating a relatively low alkalinity. This leads to minimal dissolution and then direct heteroepitaxial

https://doi.org/10.1021/jacs.3c08484
J. Am. Chem. Soc. 2023, 145, 24191−24201

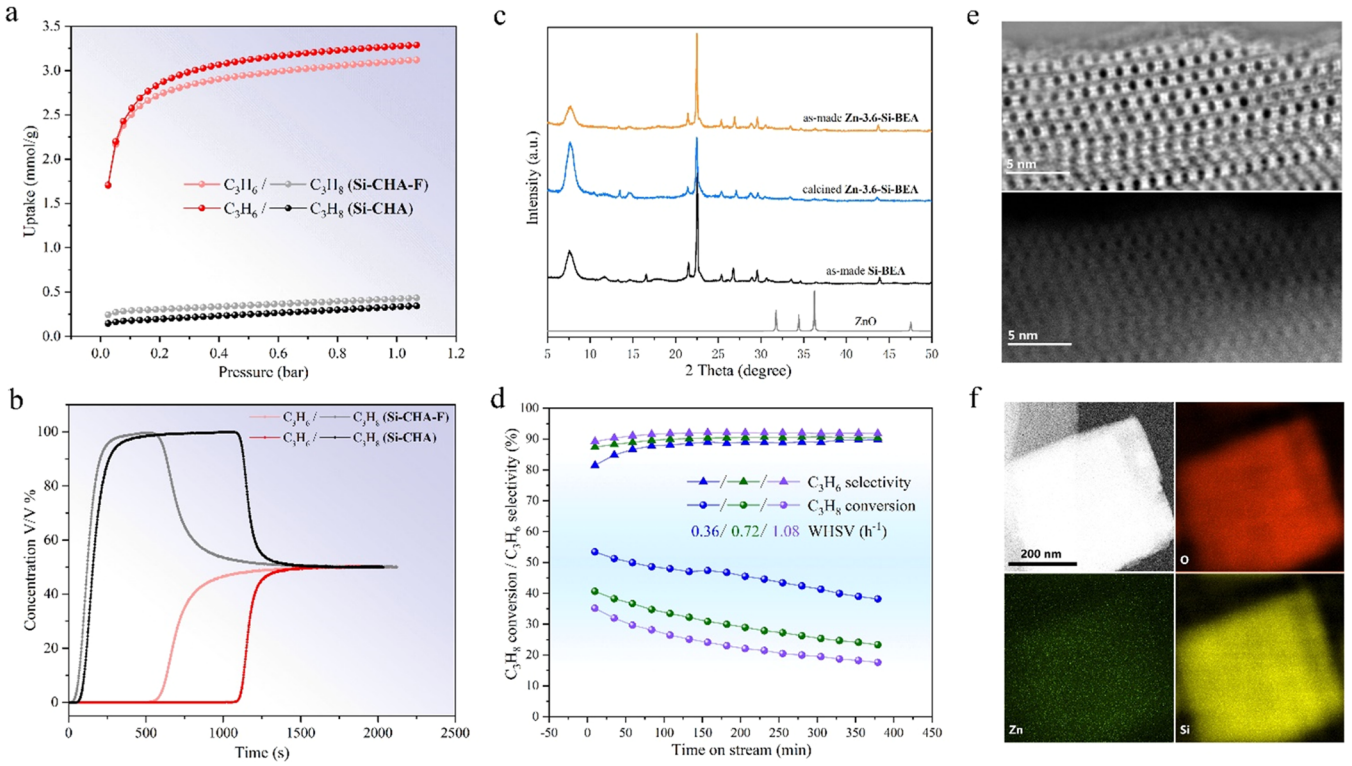

Figure 6. (a) Single-component adsorption isotherms of calcined **Si-CHA** and **Si-CHA-F** for propylene (C_3H_6) and propane (C_3H_8) measured at 298 K. (b) Breakthrough curves of calcined **Si-CHA** and **Si-CHA-F** measured under a flow of equal concentration of C_3H_6/C_3H_8 (50:50) two-component mixture at 298 K and 100 kPa. (c) PXRD patterns of as-made **Zn-3.6-Si-BEA**, calcined **Zn-3.6-Si-BEA**, as-made **Si-BEA**, and the simulated PXRD pattern of ZnO. (d) C_3H_8 conversion and C_3H_6 selectivity as a function of time on stream over the **Zn-3.6-Si-BEA** catalyst. Reaction conditions: 0.15 g of catalyst, atmospheric pressure, C_3H_8/N_2 = 1/19, 863 K, WHSV = 0.36 h^{-1}, 0.72 h^{-1}, and 1.08 h^{-1}. (e) iDPC-STEM (top) and the corresponding HAADF-STEM (bottom) images, taken along the direction of 12-ring channels, display that no apparent clusters and nanoparticles are observed in the **Zn-3.6-Si-BEA**. (f) STEM-EDS elemental mapping images of the **Zn-3.6-Si-BEA** catalyst.

growth of the **Si-CHA** phase on the surface of the parent **Si-SOD**. Moreover, we further explore the dissolution of parent **Si-SOD** in the **Si-CHA** synthesis gels with elevated alkalinity. Notably, when the $TMAdaOH/SiO_2$ molar ratio is 0.4 and after a crystallization period of 4 h, **Si-SOD** fully dissolves into a clear solution. ^{29}Si NMR of this clear solution ensures that it also possesses some amount of double 3-rings (−89.26 ppm) and *d4r*s (−98.38 ppm) siliceous species (Tables S7−S8 and Figure S26). However, the final crystallization products under the high alkalinity condition are not pure phase **Si-CHA** but contain a certain amount of layered phase impurities. It also implies that the heteroepitaxial growth pathway under the low-alkalinity conditions is more suitable for the successful synthesis of pure phase **Si-CHA**. Although **Si-CHA** and **Si-BEA** undergo different crystallization pathways, 4-rings play an important role in their successful crystallization. Thus, we speculate employing rich in 4-rings **Si-SOD** zeolites as parent materials in collaboration with the OSDA-mismatch approach is the key factor of the successful synthesis of pure-silica zeolite in the fluoride- and seed-free medium.

Propylene/Propane Separation Performance of Si-CHA Zeolite. Pure-silica zeolites have good alkane/alkene adsorption and separation performance due to their unique microporous structure, lack of acid sites, and high thermal stability.[5−7] Notably, **Si-CHA** exhibits effective adsorption for alkane/alkene separation.[42] Thus, the single-component adsorption isotherms of calcined **Si-CHA** and **Si-CHA-F** (synthesized in the fluoride medium) zeolites for propylene and propane are measured at 298 K (Figure 6a). At 298 K and 100 kPa, **Si-CHA** adsorbed up to 3.28 mmol/g of propylene, while it adsorbed only 0.34 mmol/g of propane. Furthermore, for the sake of comparison, **Si-CHA-F** is synthesized using a fluoride medium (Figure S27), yielding propylene and propane uptakes of 3.12 and 0.43 mmol/g, respectively, at a temperature of 298 K and a pressure of 100 kPa. Furthermore, the excellent separation performance of the prepared **Si-CHA** adsorbent was validated through a breakthrough experiment using an equal concentration (50:50) two-component mixture of propylene and propane, with **Si-CHA-F** as a comparison. The penetration curve results obtained from Figure 6b clearly demonstrate the separation process. Initially, propane permeates through the adsorption bed layer, followed by propylene adsorption, reaching saturation and penetrating the bed layer. In terms of retention time, propylene exhibits a remarkable retention of 1014 s on the **Si-CHA** adsorbent, while propane shows a retention time of 51 s. In contrast, the **Si-CHA-F** adsorbent demonstrates a propylene retention time of 492 s and a propane retention time of 10 s. This significant difference in retention times clearly indicates that the dynamic separation performance of propylene/propane is substantially superior for the **Si-CHA** adsorbent compared to **Si-CHA-F**.

Catalytic Performance of Zn-3.6-Si-BEA Catalyst for Propane Dehydrogenation. Propylene is an important basic feedstock used in the production of various chemicals, and propane dehydrogenation (PDH) to produce propylene has attracted increasing attention with the advantage of less side products. High-surface-area supports with abundant surface hydroxyls such as pure-silica zeolite matrices are widely used to

https://doi.org/10.1021/jacs.3c08484
J. Am. Chem. Soc. 2023, 145, 24191−24201

disperse and stabilize metal-active species of PDH.[4,43] Previous studies have conclusively shown that Zn species, which are stabilized by silanol defects in pure-silica ***BEA** zeolite obtained via the dealumination process of aluminosilicate ***BEA** zeolite, possess the catalytic activity for PDH.[44,45] The **Si-BEA** synthesized by the OSDA-mismatch approach in our research work has a large number of silanol defects and has the potential to directly be a suitable catalyst matrix for PDH. To enhance the presence of metal-active sites stabilized by additional silanol defects, the as-synthesized **Si-BEA** sample is subjected to direct exchange with a Zn^{2+} solution. The catalyst obtained after calcination contains 3.6 wt % of zinc (Zn) obtained through this exchange process (details in the Experimental Section) and displays outstanding crystallinity (Figure 6c and Table S1). It is designated as **Zn-3.6-Si-BEA** and is intended for use in the PDH reaction. UV−vis spectroscopy,[46] ^{29}Si MAS NMR,[17] STEM-EDS mapping, HAADF-STEM, and iDPC-STEM imaging results indicate that Zn species (Zn^{2+} and subnanometric ZnO clusters) in the prepared catalyst can be well dispersed in the **Si-BEA** zeolite matrix and interacted strongly with the silanol defects (Figures 6e−f and S28−S29, and Table S9). Eventually, the **Zn-3.6-Si-BEA** catalyst shows favorable activity in PDH with a conversion of propane of about ∼53% and selectivity for propylene of about ∼90% at a high temperature of 863 K and WHSV of 0.36 h^{-1} (Figure 6d). Meanwhile, increasing the WHSV exhibits a declining trend in propane conversion while concurrently enhancing the selectivity for propylene. For comparison, the catalytic activity of the **Zn-3.6-Si-BEA-F** catalyst, with its matrix synthesized using the conventional fluoride method, is presented in Figures S31−32. The **Zn-3.6-Si-BEA-F** catalyst exhibits limited activity in PDH. Overall the **Zn-3.6-Si-BEA** catalyst can simultaneously achieve high propane conversion and good stability at reasonable reaction temperatures, and it has the potential to be developed into a powerful low-cost catalyst for industrial PDH.

■ CONCLUSIONS

Designing new synthetic strategies for pure-silica zeolites under fluoride- and seed-free conditions is often a daunting task. This study showcases the effectiveness of the OSDA-mismatch approach in the simple and rapid synthesis of 15 pure-silica zeolites (**CHA**, **BEA**, **EUO**, **SFF**, **STF**, **-SVR**, ***-SVY**, **DOH**, **MTN**, **NON**, ***MRE**, **MEL**, **MFI**, **MTW**, and ***STO**) without the need for fluorides or seedings. The distinct crystallization pathways were observed for two significant **Si-CHA** and **Si-BEA** zeolites through the OSDA-mismatch approach. Additionally, **Si-CHA** and **Si-BEA** synthesized through this approach exhibit excellent thermal stability and contain silanol defects, making them highly effective adsorbents and matrices. More importantly, the utilization of this unique synthetic approach is expected to facilitate the discovery of novel pure-silica zeolites with fascinating topologies.

■ EXPERIMENTAL SECTION

Ingredients. Solid silica gel (SiO_2, 98%, Qingdao Haiyang Chemical Reagent), sodium metasilicate nonahydrate ($Na_2SiO_3·9H_2O$, 98%, Macklin), ethylene glycol (EG, 98%, Tianjin Damao Chemical Reagent), tetramethylammonium hydroxide (TMAOH, 25%, Shanghai Aladdin), *N*,*N*,*N*-trimethyl-1-adamantammonium hydroxide (TMAdaOH, 20%, SACHEM), benzyltrimethylammonium hydroxide (BnTMAOH, 40%, Shanghai Aladdin), tetraethylammonium hydroxide (TEAOH, 35%, Shanghai Aladdin), tetrapropylammonium hydroxide (TPAOH, 25%, Shanghai Aladdin), tetrabutylammonium hydroxide (TBAOH, 40%, Shanghai Aladdin), hexamethonium bromide ($HMBr_2$, 98%, Shanghai Aladdin), 1,3-bis(cyclohexyl)imidazolium chloride (1,3-Dcyh-MICl, 98%, Shanghai Aladdin), 1,2,2,6,6-pentamethylpiperidinium hydroxide (1,2,2,6,6-PMePDOH, 98%, Shanghai Aladdin), silver oxide (Ag_2O, 99.7%, Shanghai Aladdin), *N*-methylpyrrolidine (98%, Shanghai Aladdin), 1,4-dibromobutane (98%, Shanghai Aladdin), 1,6-dibromohexane (97%, Shanghai Aladdin), 1,4-diiodobutane (98%, Shanghai Aladdin), trimethylamine (30%, Shanghai Aladdin), iodoethane (98%, Shanghai Aladdin), iodomethane (98%, Shanghai Aladdin), cis-2,6-dimethylpiperidine (97%, Shanghai Aladdin), 2-ethyl-4-methylimidazole (96%, Shanghai Aladdin), 1-cyclohexylpiperazine (98%, Shanghai Aladdin), tris(dimethylamino)phosphine (97%, Shanghai Aladdin), ethanol (99.5%, Kermel), acetone (99.5%, DAMAO), acetonitrile (99.5%, XIHUA), diethyl ether (99.7%, Sinopharm), methanol (99.5%, Sinopharm), potassium bicarbonate ($KHCO_3$, 99.5%, Shanghai Aladdin), potassium carbonate (K_2CO_3, 99%, Shanghai Aladdin), chloroform (99%, XIHUA), hydrochloric acid (HCl, 37%, Kermel), hydrofluoric acid (HF, 40%, Kermel), tetraethoxysilane (TEOS, 98%, Kermel), $Zn(NO_3)_2·6H_2O$ (99%, Shanghai Aladdin), and deuterium oxide (D_2O, 99.9%, Leyan).

Preparation of Starting Material Si-SOD. The starting material, **Si-SOD**, was prepared according to a previously reported solvent-free synthesis method with a molar composition of $SiO_2/Na_2SiO_3·9H_2O$/EG= 1.00:0.07:1.66.[47] The solid silica gel and sodium metasilicate nonahydrate were homogeneously mixed by grinding under dry room temperature, and then ethylene glycol was added and continuously ground for 10 min until a viscous solid was formed. Subsequently, the viscous solid was transferred to the autoclave and sealed well. After crystallization in a static oven at a constant temperature of 200 °C for 24 to 48 h, the crystallized solid product was washed by centrifugation and dried overnight at 100 °C to obtain the starting material **Si-SOD**.

Preparation for OSDAs. TMAOH, TMAdaOH, TEAOH, TPAOH, TBAOH, BnTMAOH, and 1,2,2,6,6-PMePDOH were obtained directly through the commercial procurement route.

$HM(OH)_2$ and 1,3-Dcyh-MIOH were obtained by exchanging commercialized $HMBr_2$ and 1,3-Dcyh-MICl with silver oxide for 4 h while avoiding exposure to light.

Hexamethylene-1,6-bis(*N*-methyl-*N*-pyrrolidinium) dibromide salt (1,6-$MPHBr_2$) was prepared by reacting 1,6-dibromohexane with an excess of *N*-methylpyrrolidine in acetone as the solvent with rapid stirring at room temperature for 3 days. The white solid product was centrifuged, washed with acetone, and recrystallized with ethanol to obtain the pure 1,6-$MPHBr_2$. Then, 1,6-$MPHBr_2$ was exchanged to 1,6-$MPH(OH)_2$ with silver oxide for 4 h under avoidance of light.

1,4-Butanediylbis[tris(dimethylamino)]phosphonium diiodide salt (1,4-$TDEAPI_2$) was prepared by adding a solution of 31.1 g (100 mmol) of 1,4-diiodobutane in 75 mL of acetonitrile dropwise under stirring into a solution of 40.8 g (250 mmol) of tris(dimethylamino)-phosphine in 75 mL of acetonitrile. The resulting mixture was stirred at room temperature for 2 days. The white precipitate was recovered by filtration, washed with acetonitrile and diethyl ether, and dried under a vacuum to obtain pure 1,4-$TDEAPI_2$. Subsequently, 1,4-$TDEAPI_2$ was converted to 1,4-$TDEAP(OH)_2$ through an exchange with silver oxide for 4 h while avoiding exposure to light.

1,1-Diethyl-cis-2,6-dimethylpiperidinium iodide salt (DEDMPI) was prepared by reacting cis-2,6-dimethylpiperidine, iodoethane, and an excess of $KHCO_3$ in the presence of methanol solvent, followed by refluxing at 70 °C for 4 days. The $KHCO_3$ was filtered, and then the solvent and the excess of iodoethane were removed by rotary evaporation. The product was washed with ether. The white solid product was washed with ether to obtain pure DEDMPI. Subsequently, DEDMPI was exchanged to DEDMPOH with silver oxide for 4 h while avoiding exposure to light.

1,2,3-Triethyl-4-methylimidazolium iodide salt (1,2,3-TE-4M-MI) was prepared by 2-ethyl-4-methylimidazole with an excess of iodoethane, and potassium carbonate sesquihydrate was dissolved in chloroform. The solution was stirred for 2 days at room temperature. Then, a second portion of iodoethane (same proportion) was added.

https://doi.org/10.1021/jacs.3c08484
J. Am. Chem. Soc. 2023, 145, 24191−24201

The resulting mixture was magnetically stirred for 4 days. The inorganic phase was separated from the mother solution by filtration, and the desired product 1,2,3-TE-4M-MI was obtained by rotatory evaporation under vacuum. Subsequently, 1,2,3-TE-4M-MI was converted to 1,2,3-TE-4M-MOH by exchanging it with silver oxide for 4 h while avoiding exposure to light.

4-Cyclohexyl-1,1-dimethyl-piperazinium iodide salt (1,1-DM-4-cyhPZI) was prepared by *N*-cyclohexylpiperazine with iodomethane. The detailed description is the following: 15.0 g (89 mmol) of *N*-cyclohexylpiperazine and 12.3 g (89 mmol) of K_2CO_3 were dissolved in 300 mL of acetone. Subsequently, 51.0 g (359 mmol) of iodomethane was slowly added and the mixture was stirred at room temperature for 1 day. After that, the solvent was evaporated under vacuum, diethyl ether was added, and a solid was obtained. The solid was submitted to Soxhlet extraction with chloroform as solvent overnight. The suspension was concentrated under vacuum and the complete precipitation of the salt was achieved by the addition of diethyl ether. The solid was recovered by filtration, washed with diethyl ether, and dried under vacuum to obtain the pure 1,1-DM-4-cyhPZI. Subsequently, 1,1-DM-4-cyhPZI was exchanged to 1,1-DM-4-cyhPZOH with silver oxide for 4 h while avoiding exposure to light.

1,4-Bis(*N*-methylpyrrolidinium)butane dibromide salt (1,4-MPBBr$_2$) was prepared by reacting 1,4-dibromobutane with an excess of *N*-methylpyrrolidine in acetone as the solvent with rapid stirring at room temperature for 1 day. The white solid product was centrifuged, washed with acetone, and recrystallized with ethanol to obtain the pure 1,4-MPBBr$_2$. Then 1,4-MPBBr$_2$ was exchanged to 1,4-MPB-(OH)$_2$ with silver oxide for 4 h while avoiding exposure to light.

1,4-Bis(trimethylamino)butane dibromide salt (HM-C$_4$Br$_2$) was prepared by reacting 1,4-dibromobutane with an excess of trimethylamine in methanol as the solvent with rapid stirring at room temperature for 7 days. The white solid product was centrifuged and washed with ethanol to obtain pure HM-C$_4$Br$_2$. Then, HM-C$_4$Br$_2$ was exchanged to HM-C$_4$(OH)$_2$ with silver oxide for 4 h while avoiding exposure to light.

The molecular structures of OSDAs were verified by using ^{1}H and ^{13}C nuclear magnetic resonance (NMR). The concentration of OSDAs hydroxide in the aqueous solutions was determined by titration with 0.1 M hydrochloric acid.

Synthesis of Pure-Silica Zeolites in the Fluoride- and Seed-Free System. Pure-silica zeolites were synthesized hydrothermally using gel molar compositions of 1.00 SiO_2:6.00−20.00 H_2O:0.10−0.50 OSDA, with the corresponding OSDAs employed. The synthesis conditions are provided in Table 1, outlining the specific details. Therein, the starting material **Si-SOD** exclusively served as the silicon source (SiO_2) in these synthesis processes.

In a typical fluoride- and seed-free synthesis of pure-silica zeolites, the procedure involves stirring a specific amount of **Si-SOD** with the corresponding OSDA in a Teflon-lined autoclave at room temperature for 3 h. The excess water is then evaporated using a constant temperature water bath set at 80 °C to achieve a suitable H_2O/SiO_2 ratio. The autoclave is sealed and placed in a rotating oven, maintained at a temperature range of 150−175 °C, and rotated at 30 rpm for a predetermined period of time. Following the crystallization process, the autoclave is cooled to room temperature using flowing water, and the resulting solid sample is obtained by centrifugation. It is then washed with deionized water and dried overnight at 100 °C.

Preparation of Si-CHA-F in the Fluoride System. Pure-silica **Si-CHA-F** zeolites were synthesized hydrothermally in the presence of fluorine ions, using a gel molar composition of 1.00 SiO_2:3.00 H_2O:0.75 TMAdaOH:0.75 HF and used as the comparison sample.[27] TEOS was stirred with TMAdaOH in a Teflon-lined autoclave overnight at room temperature. The excess water was then evaporated in a constant temperature water bath set at 80 °C to achieve a suitable H_2O/SiO_2 ratio. HF was added dropwise to the resulting gel while being manually stirred until it became thick and uniform. The autoclave was sealed and placed in a rotating oven operating at 140 °C for 5 days at 50 rpm. After the crystallization process, the autoclave was cooled to room temperature by using flowing water. The resulting solid sample was then separated by centrifugation, washed with deionized water, and dried overnight at 100 °C.

Preparation of Zn-3.6-Si-BEA Catalyst. **Zn-3.6-Si-BEA** catalyst is prepared by the direct ion exchange of the as-made **Si-BEA** sample using 0.1 M $Zn(NO_3)_2$ solution at 80 °C for 4 h, followed by drying at 80 °C overnight and calcining at 550 °C in air for 4 h.

Characterizations. The crystallinity and phase purity of all samples were determined by collecting and analyzing PXRD data on a PANalytical X'Pert PRO X-ray diffractometer with CuKα radiation (λ = 1.5418 Å) in Bragg−Brentano geometry. Scanning electron microscopy (SEM) images were obtained on a Hitachi SU8020 microscope with an accelerating voltage of 2 kV. Thermogravimetric analysis (TGA) was characterized using a TA Q-600 analyzer with a heating rate of 10 °C/min under flowing air condition. The specific surface areas (BET) and micropore volume were obtained by using a Micromeritics 3Flex analyzer at 77 K. Before the adsorption, the calcined zeolite was activated for 4 h at 623 K. BET and pore size distribution were evaluated by the adsorption branch, respectively. Liquid-state ^{29}Si NMR was collected on a Bruker Avance 400 spectrometer at a resonance frequency of 79.48 MHz. An appropriate amount of the solution (0.5 mL) was then loaded into a 5 mm NMR quartz tube (Wilmad), and a small amount of D_2O sealed in a capillary tube was added in the quartz tube for a lock signal. 102,400 scans were accumulated with a 1 s recycle delay. The solid-state NMR experiments were conducted by using a Bruker Avance III 600 spectrometer equipped with a 14.1 T wide-bore magnet and a 4 mm WVT double-resonance MAS probe. The resonance frequencies of ^{1}H, ^{13}C, and ^{29}Si are 600.13, 150.9, and 119.2 MHz, respectively. ^{13}C MAS NMR spectra were recorded using a cross-polarization (CP, ^{1}H → ^{13}C) sequence with a contact time of 3 ms and a recycle delay of 2 s at a spinning rate of 12 kHz. 1024 scans were accumulated to achieve a satisfactory signal-to-noise ratio. The chemical shifts were referenced to adamantane with the upfield methine peak at 29.5 ppm. ^{29}Si MAS NMR spectra were recorded with a spinning rate of 8 kHz using high-power proton decoupling. 800 scans were accumulated with a recycle delay of 60 s recycle delay. Chemical shifts were referenced to kaolinite at −91.5 ppm. IR spectra were collected on a Bruker Tensor 27 instrument equipped with an MCT detector after the samples were pretreated at 300 °C for 60 min in vacuum. Self-supported wafers of both samples (20 mg) were placed into an in situ quartz cell equipped with CaF_2 windows. The Zn content was determined using PANalytical Axios Advanced X-ray fluorescence spectroscopy (XRF). Diffuse reflectance UV−vis spectra were recorded in the range of 200−800 nm using a VARIAN Cary-5000 UV−vis−NIR spectrophotometer with a $BaSO_4$ reference standard. Propylene temperature-programmed desorption (C_3H_6-TPD-MS) measurement was performed on a chemisorption analyzer (Micromeritics AutoChem II 2920) connected with mass spectrometry (OmniStar 300). 0.15 g of catalyst was reduced with 10 vol % H_2/Ar gas (20 mL min^{-1}) at 600 °C for 1 h and then purged in Ar flowing (20 mL min^{-1}) for 30 min. When cooled to 100 °C, 5% C_3H_6/Ar (20 mL min^{-1}) was passed through the reduced catalyst for 30 min and then purged in an Ar flow (20 mL min^{-1}). Ultimately, the catalyst with adsorbed propylene was heated to 590 °C at a heating rate of 10 °C min^{-1}. The desorbed products were measured by online MS.

The specimens for transmission electron microscopy (TEM) were prepared by a Helios 5 cx FIB dual beam microscope. First, the electron beam current and voltage were adjusted to achieve balance and quickly locate a crystal with the appropriate orientation under the optimized conditions of 3 kV and 21 pA. Next, the selected crystal was transferred onto the TEM grid and Pt deposition was carried out on its surface to provide protection. The crystal was initially sectioned to approximately 3 μm using a Ga$^+$ ion beam (30 kV, 2.5 nA) and subsequently milled down to 1 μm and 150 nm at ion beam currents of 0.43 nA and 0.23 nA, respectively. Finally, the specimen was further thinned to a thickness of less than 100 nm at 5 kV and 68 pA. The cRED data were collected on a JEOL 2100plus equipped with an ASI Cheetah120 detector at 200 kV, and the 3D reciprocal lattice was reconstructed by REDp software. Four-dimensional scanning transmission electron microscopy (4D-STEM) and high-resolution

https://doi.org/10.1021/jacs.3c08484
J. Am. Chem. Soc. 2023, 145, 24191−24201

transmission electron microscopy (HRTEM) were performed on a spherical aberration-corrected Spectra 300 transmission electron microscope operated at 300 kV with a OneView CMOS camera. High-angle annular dark-field scanning transmission electron microscopy (HAADF-STEM) and integrated differential phase-contrast (iDPC) images were recorded on FEI Titan Cubed Themis ETEM G3. STEM-energy-dispersive spectroscopy (STEM-EDS) elemental mapping images were recorded on a JEOL JEM-ARM300F microscope at 300 kV.

Adsorption Measurements. The single-component adsorption isotherms of propylene and propane of all adsorbents were performed on a Micromeritics 3Flex adsorption apparatus at 298 K. Before the adsorption, these calcined **Si-CHA** and **Si-CHA-F** zeolites used as adsorbents were activated for 4 h at 623 K. The propylene and propane used in the tests were high-purity gases and did not undergo any purification. Breakthrough experiments were performed on the BEISHIDE BSD-MAB multicomponent competitive adsorption penetration curve analyzer. The mixed gases used in the breakthrough experiments were divided into equal concentrations of propylene (50%, V/V) and propane (50%, V/V). The adsorption column, which was 6.0 mm in diameter and 58.0 mm in length, was filled with 0.7 g of adsorbent. Prior to the measurements, these adsorbents were activated by in situ vacuum heating at 350 °C for 4 h. Breakthrough experiments were performed at 298 K with a feed gas pressure of 101 kPa flowing at 5 mL/min.

Catalytic Measurements. The propane dehydrogenation reaction was carried out in a quartz fixed-bed reactor with an inner diameter of 6 mm at atmospheric pressure. First, a catalyst sample (typically 0.15 g, sieve fraction of 60−80 mesh) was placed in the quartz reactor and treated with 30 vol % H_2 for 30 min, followed by pure N_2 for 30 min, both at 873 K. The reactant gas mixture, consisting of 5 vol % propane with the balance N_2, was fed into the reactor, and the reaction temperature was maintained at 863 K. The weight hourly space velocity (WHSV) of propane was controlled at 0.36, 0.72, and 1.08 h^{-1}. The reaction was conducted under isothermal conditions, and the gas products were analyzed by using an online gas chromatograph (Agilent 7890B). The conversion of propane and the selectivity toward propylene were defined as follows:

$$C_3H_8 \text{ conversion } (\%) = \frac{[C_3H_8]_{inlet} - [C_3H_8]_{outlet}}{[C_3H_8]_{inlet}} \times 100$$

$$C_3H_6 \text{ selectivity } (\%) = \frac{[C_3H_6]_{outlet}}{[C_3H_8]_{inlet} - [C_3H_8]_{outlet}} \times 100$$

■ ASSOCIATED CONTENT

Supporting Information

The Supporting Information is available free of charge at https://pubs.acs.org/doi/10.1021/jacs.3c08484.

Notes and OSDAs for materials preparation, PXRD, SEM, solid-state ^{29}Si MAS NMR, HRTEM, HAADF-STEM, UV−vis, and other additional information (PDF)

■ AUTHOR INFORMATION

Corresponding Authors

Peng Guo − *National Engineering Research Center of Lower-Carbon Catalysis Technology, Dalian Institute of Chemical Physics, Chinese Academy of Sciences, Dalian 116023 Liaoning, China; University of Chinese Academy of Sciences, Beijing 100049, China;* orcid.org/0000-0001-5392-3915; Email: pguo@dicp.ac.cn

Zhongmin Liu − *National Engineering Research Center of Lower-Carbon Catalysis Technology, Dalian Institute of Chemical Physics, Chinese Academy of Sciences, Dalian 116023 Liaoning, China; University of Chinese Academy of Sciences, Beijing 100049, China; School of Chemistry, Dalian University of Technology, Dalian 116024 Liaoning, China;* Email: zml@dicp.ac.cn

Authors

Chao Ma − *National Engineering Research Center of Lower-Carbon Catalysis Technology, Dalian Institute of Chemical Physics, Chinese Academy of Sciences, Dalian 116023 Liaoning, China; University of Chinese Academy of Sciences, Beijing 100049, China; School of Chemistry, Dalian University of Technology, Dalian 116024 Liaoning, China*

Xiaona Liu − *National Engineering Research Center of Lower-Carbon Catalysis Technology, Dalian Institute of Chemical Physics, Chinese Academy of Sciences, Dalian 116023 Liaoning, China*

Yang Hong − *National Engineering Research Center of Lower-Carbon Catalysis Technology, Dalian Institute of Chemical Physics, Chinese Academy of Sciences, Dalian 116023 Liaoning, China; University of Chinese Academy of Sciences, Beijing 100049, China*

Nana Yan − *National Engineering Research Center of Lower-Carbon Catalysis Technology, Dalian Institute of Chemical Physics, Chinese Academy of Sciences, Dalian 116023 Liaoning, China*

Chenyang Nie − *National Engineering Research Center of Lower-Carbon Catalysis Technology, Dalian Institute of Chemical Physics, Chinese Academy of Sciences, Dalian 116023 Liaoning, China; University of Chinese Academy of Sciences, Beijing 100049, China*

Jing Wang − *National Engineering Research Center of Lower-Carbon Catalysis Technology, Dalian Institute of Chemical Physics, Chinese Academy of Sciences, Dalian 116023 Liaoning, China;* orcid.org/0000-0002-4185-0373

Complete contact information is available at: https://pubs.acs.org/10.1021/jacs.3c08484

Author Contributions

The manuscript was written through contributions of all authors. All authors have given approval to the final version of the manuscript.

Notes

The authors declare no competing financial interest.

■ ACKNOWLEDGMENTS

This work was supported by the National Natural Science Foundation of China (nos. 22288101, 21972136, 21991090, 21991091, and 22102177). The authors express their heartfelt gratitude to Professor Daliang Zhang, Yujiao Wang, and Jia Lv from Chongqing University for their invaluable assistance in the FIB and HRTEM processes. They also thank Associate Professor Jingfeng Han at the Dalian Institute of Chemical Physics for his support and guidance in the Raman test. Furthermore, they appreciate the contribution of Associate Professor Dong Fan from the Dalian Institute of Chemical Physics for his help in the IR characterization.

■ REFERENCES

(1) Hu, Z.-P.; Qin, G.; Han, J.; Zhang, W.; Wang, N.; Zheng, Y.; Jiang, Q.; Ji, T.; Yuan, Z.-Y.; Xiao, J.; Wei, Y.; Liu, Z. Atomic Insight into the Local Structure and Microenvironment of Isolated Co-Motifs in MFI Zeolite Frameworks for Propane Dehydrogenation. *J. Am. Chem. Soc.* **2022**, *144* (27), 12127−12137.

(2) Liu, L.; Díaz, U.; Arenal, R.; Agostini, G.; Concepción, P.; Corma, A. Generation of Subnanometric Platinum with High Stability during Transformation of a 2D Zeolite into 3D. *Nat. Mater.* **2017**, *16* (1), 132−138.
(3) Sun, Q.; Wang, N.; Fan, Q.; Zeng, L.; Mayoral, A.; Miao, S.; Yang, R.; Jiang, Z.; Zhou, W.; Zhang, J.; Zhang, T.; Xu, J.; Zhang, P.; Cheng, J.; Yang, D.; Jia, R.; Li, L.; Zhang, Q.; Wang, Y.; Terasaki, O.; Yu, J. Subnanometer Bimetallic Platinum−Zinc Clusters in Zeolites for Propane Dehydrogenation. *Angew. Chem., Int. Ed* **2020**, *59* (44), 19450−19459.
(4) Chai, Y.; Shang, W.; Li, W.; Wu, G.; Dai, W.; Guan, N.; Li, L. Noble Metal Particles Confined in Zeolites: Synthesis, Characterization, and Applications. *Adv. Sci.* **2019**, *6* (16), No. 1900299.
(5) Wang, J.; Ma, C.; Liu, J.; Liu, Y.; Xu, X.; Xie, M.; Wang, H.; Wang, L.; Guo, P.; Liu, Z. Pure Silica with Ordered Silanols for Propylene/Propane Adsorptive Separation Unraveled by Three-Dimensional Electron Diffraction. *J. Am. Chem. Soc.* **2023**, *145* (12), 6853−6860.
(6) Bereciartua, P. J.; Cantín, Á.; Corma, A.; Jordá, J. L.; Palomino, M.; Rey, F.; Valencia, S.; Corcoran, E. W.; Kortunov, P.; Ravikovitch, P. I.; Burton, A.; Yoon, C.; Wang, Y.; Paur, C.; Guzman, J.; Bishop, A. R.; Casty, G. L. Control of Zeolite Framework Flexibility and Pore Topology for Separation of Ethane and Ethylene. *Science* **2017**, *358* (6366), 1068−1071.
(7) Park, J.; Cho, K. H.; Kim, J.-C.; Ryoo, R.; Park, J.; Lee, Y.; Choi, M. Design of Olefin-Phobic Zeolites for Efficient Ethane and Ethylene Separation. *Chem. Mater.* **2023**, *35* (5), 2078−2087.
(8) Wang, Z.; Wang, H.; Mitra, A.; Huang, L.; Yan, Y. Pure-Silica Zeolite Low-k Dielectric Thin Films. *Adv. Mater.* **2001**, *13* (10), 746−749.
(9) Baerlocher, Ch. Database of Zeolite Structures. https://asia.iza-structure.org/IZA-SC/ftc_table.php (accessed Aug 30, 2022).
(10) Ma, C.; Liu, X.; Nie, C.; Chen, L.; Tian, P.; Xu, H.; Guo, P.; Liu, Z. Applications of X-Ray and Electron Crystallography in Structural Investigations of Zeolites. *Chem. J. Chin. Univ.* **2021**, *42* (1), 188−200, DOI: 10.7503/cjcu20200406.
(11) Guo, P.; Yan, N.; Wang, L.; Zou, X. Database Mining of Zeolite Structures. *Cryst. Growth Des.* **2017**, *17* (12), 6821−6835.
(12) Luo, D.; Wang, Q.; Fan, D.; Yang, M.; Fan, B.; Cao, K.; Xu, S.; Tian, P.; Liu, Z. Hydrothermal Synthesis of Siliceous Beta Zeolite by an Inorganic Cation-Driven Strategy and Its Crystallization Mechanism. *Microporous Mesoporous Mater.* **2022**, *329*, No. 111557.
(13) Yu, X.; Meng, S.; Liu, S.; Yang, Y.; Liu, B.; Zhu, L.; Cao, X. Fluoride-Free Synthesis of Beta Zeolite with Enrichment of Polymorph B from a Solvent-Free Route. *Dalton Trans.* **2022**, *51* (10), 3845−3848.
(14) Yang, Y.; Meng, X.; Zhu, L.; Yang, J.; Zhang, G.; Shen, H.; Cao, X. Rapid Synthesis of Si-Rich SSZ-13 Zeolite under Fluoride-Free Conditions. *Inorg. Chem.* **2022**, *61* (51), 21115−21122.
(15) Wu, Q.; Zhu, L.; Chu, Y.; Liu, X.; Zhang, C.; Zhang, J.; Xu, H.; Xu, J.; Deng, F.; Feng, Z.; Meng, X.; Xiao, F. Sustainable Synthesis of Pure Silica Zeolites from a Combined Strategy of Zeolite Seeding and Alcohol Filling. *Angew. Chem., Int. Ed.* **2019**, *58* (35), 12138−12142.
(16) Zhu, Z.; Xu, H.; Jiang, J.; Wu, H.; Wu, P. Hydrophobic Nanosized All-Silica Beta Zeolite: Efficient Synthesis and Adsorption Application. *ACS Appl. Mater. Interfaces* **2017**, *9* (32), 27273−27283.
(17) Vattipalli, V.; Paracha, A. M.; Hu, W.; Chen, H.; Fan, W. Broadening the Scope for Fluoride-Free Synthesis of Siliceous Zeolites. *Angew. Chem., Int. Ed.* **2018**, *57* (14), 3607−3611.
(18) Ma, Z.; Deng, H.; Li, L.; Zhang, Q.; Chen, G.; Sun, C.; He, H.; Yu, J. Fluoride-Free and Seed-Free Microwave-Assisted Hydrothermal Synthesis of Nanosized High-Silica Beta Zeolites for Effective VOCs Adsorption. *Chem. Sci.* **2023**, *14* (8), 2131−2138.
(19) Shao, Y.; Wang, L.; Zhang, J.; Anpo, M. Novel Synthesis of High Hydrothermal Stability and Long-Range Order MCM-48 with a Convenient Method. *Microporous Mesoporous Mater.* **2005**, *86* (1−3), 314−322.
(20) Fischer, M. Influence of Organic Structure-Directing Agents on Fluoride Dynamics in As-Synthesized Silicalite-1. *J. Phys. Chem. C* **2020**, *124* (10), 5690−5701.
(21) Fischer, M. Fluoride Anions in All-Silica Zeolites: Studying Preferred Fluoride Sites and Dynamic Disorder with Density Functional Theory Calculations. *J. Phys. Chem. C* **2021**, *125* (16), 8825−8839.
(22) Bregante, D. T.; Potts, D. S.; Kwon, O.; Ayla, E. Z.; Tan, J. Z.; Flaherty, D. W. Effects of Hydrofluoric Acid Concentration on the Density of Silanol Groups and Water Adsorption in Hydrothermally Synthesized Transition-Metal-Substituted Silicalite-1. *Chem. Mater.* **2020**, *32* (17), 7425−7437.
(23) Arranz, M.; Pérez-Pariente, J.; Wright, P. A.; Slawin, A. M. Z.; Blasco, T.; Gómez-Hortigüela, L.; Corà, F. Cooperative Structure-Directing Effect of Fluorine-Containing Organic Molecules and Fluoride Anions in the Synthesis of Zeolites. *Chem. Mater.* **2005**, *17* (17), 4374−4385.
(24) Fyfe, C. A.; Brouwer, D. H.; Lewis, A. R.; Villaescusa, L. A.; Morris, R. E. Combined Solid State NMR and X-Ray Diffraction Investigation of the Local Structure of the Five-Coordinate Silicon in Fluoride-Containing As-Synthesized STF Zeolite. *J. Am. Chem. Soc.* **2002**, *124* (26), 7770−7778.
(25) Baerlocher, C.; Xie, D.; McCusker, L. B.; Hwang, S.-J.; Chan, I. Y.; Ong, K.; Burton, A. W.; Zones, S. I. Ordered Silicon Vacancies in the Framework Structure of the Zeolite Catalyst SSZ-74. *Nat. Mater.* **2008**, *7* (8), 631−635.
(26) Smeets, S.; Berkson, Z. J.; Xie, D.; Zones, S. I.; Wan, W.; Zou, X.; Hsieh, M.-F.; Chmelka, B. F.; McCusker, L. B.; Baerlocher, C. Well-Defined Silanols in the Structure of the Calcined High-Silica Zeolite SSZ-70: New Understanding of a Successful Catalytic Material. *J. Am. Chem. Soc.* **2017**, *139* (46), 16803−16812.
(27) Cosseron, A.-F.; Daou, T. J.; Tzanis, L.; Nouali, H.; Deroche, I.; Coasne, B.; Tchamber, V. Adsorption of Volatile Organic Compounds in Pure Silica CHA, *BEA, MFI and STT-Type Zeolites. *Microporous Mesoporous Mater.* **2013**, *173*, 147−154.
(28) Darton, R. J.; Brouwer, D. H.; Fyfe, C. A.; Villaescusa, L. A.; Morris, R. E. Solid-State NMR Studies of the Fluoride-Containing Zeolite SSZ-44. *Chem. Mater.* **2004**, *16* (4), 600−603.
(29) Xue, C.; Xu, T. Fluorine-Free Synthesis of Large ZSM-39 Crystals Incorporated with Alkaline Earth Metals in an Environment-Friendly System. *Mater. Lett.* **2013**, *112*, 200−202.
(30) Arranz, M.; Pérez-Pariente, J.; Blasco, T. Fluorine-Containing Organic Molecules as Structure-Directing Agents in the Synthesis of Crystalline Microporous Materials. Part II: Synthesis of All-Silica Zeolites from Fluorine-Containing Derivatives of 1-Benzyl-1-Methyl-Hexamethylenammonium Cations. *Microporous Mesoporous Mater.* **2006**, *89* (1−3), 235−245.
(31) Vortmann, S.; Marler, B.; Gies, H.; Daniels, P. Synthesis and Crystal Structure of the New Borosilicate Zeolite RUB-13. *Microporous Mater.* **1995**, *4* (2−3), 111−121.
(32) Suzuki, K.; Hayakawa, T. The Effects of Seeding in the Synthesis of Zeolite ZSM-48 in the Presence of Tetramethylammonium Ion. *Microporous Mesoporous Mater.* **2005**, *77* (2−3), 131−137.
(33) Zones, S. I.; Nakagawa, Y.; Yuen, L. T.; Harris, T. V. Guest/Host Interactions in High Silica Zeolite Synthesis: [5.2.1.0 ^{2,6}]Tricyclodecanes as Template Molecule. *J. Am. Chem. Soc.* **1996**, *118* (32), 7558−7567.
(34) Piccione, P. M.; Davis, M. E. A New Structure-Directing Agent for the Synthesis of Pure-Phase ZSM-11. *Microporous Mesoporous Mater.* **2001**, *49* (1−3), 163−169.
(35) Watanabe, R.; Yokoi, T.; Tatsumi, T. Synthesis and Application of Colloidal Nanocrystals of the MFI-Type Zeolites. *J. Colloid Interface Sci.* **2011**, *356* (2), 434−441.
(36) Tzanis, L.; Trzpit, M.; Soulard, M.; Patarin, J. High Pressure Water Intrusion Investigation of Pure Silica 1D Channel AFI, MTW and TON-Type Zeolites. *Microporous Mesoporous Mater.* **2011**, *146* (1−3), 119−126.
(37) Minami, A.; Hu, P.; Sada, Y.; Yamada, H.; Ohara, K.; Yonezawa, Y.; Sasaki, Y.; Yanaba, Y.; Takemoto, M.; Yoshida, Y.;

Okubo, T.; Wakihara, T. Tracking Sub-Nano-Scale Structural Evolution in Zeolite Synthesis by *In Situ* High-Energy X-Ray Total Scattering Measurement with Pair Distribution Function Analysis. *J. Am. Chem. Soc.* **2022**, *144* (51), 23313−23320.
(38) Park, M. B.; Lee, Y.; Zheng, A.; Xiao, F.-S.; Nicholas, C. P.; Lewis, G. J.; Hong, S. B. Formation Pathway for LTA Zeolite Crystals Synthesized via a Charge Density Mismatch Approach. *J. Am. Chem. Soc.* **2013**, *135* (6), 2248−2255.
(39) Grand, J.; Awala, H.; Mintova, S. Mechanism of Zeolites Crystal Growth: New Findings and Open Questions. *CrystEngComm* **2016**, *18* (5), 650−664.
(40) Cheng, C.-H.; Shantz, D. F. ^{29} Si NMR Studies of Zeolite Precursor Solutions. *J. Phys. Chem. B* **2006**, *110* (1), 313−318.
(41) Castro, M.; Haouas, M.; Lim, I.; Bongard, H. J.; Schüth, F.; Taulelle, F.; Karlsson, G.; Alfredsson, V.; Breyneart, E.; Kirschhock, C. E. A.; Schmidt, W. Zeolite Beta Formation from Clear Sols: Silicate Speciation, Particle Formation and Crystallization Monitored by Complementary Analysis Methods. *Chem. - Eur. J.* **2016**, *22* (43), 15307−15319.
(42) Olson, D. H.; Camblor, M. A.; Villaescusa, L. A.; Kuehl, G. H. Light Hydrocarbon Sorption Properties of Pure Silica Si-CHA and ITQ-3 and High Silica ZSM-58. *Microporous Mesoporous Mater.* **2004**, *67* (1), 27−33.
(43) Liu, J.; Liu, Y.; Liu, H.; Fu, Y.; Chen, Z.; Zhu, W. Silicalite-1 Supported ZnO as an Efficient Catalyst for Direct Propane Dehydrogenation. *ChemCatChem* **2021**, *13* (22), 4780−4786.
(44) Chen, C.; Hu, Z.; Ren, J.; Zhang, S.; Wang, Z.; Yuan, Z.-Y. ZnO Nanoclusters Supported on Dealuminated Zeolite β as a Novel Catalyst for Direct Dehydrogenation of Propane to Propylene. *ChemCatChem* **2019**, *11* (2), 868−877.
(45) Xie, L.; Chai, Y.; Sun, L.; Dai, W.; Wu, G.; Guan, N.; Li, L. Optimizing Zeolite Stabilized Pt-Zn Catalysts for Propane Dehydrogenation. *J. Energy Chem.* **2021**, *57*, 92−98.
(46) Nozik, D.; Tinga, F. M. P.; Bell, A. T. Propane Dehydrogenation and Cracking over Zn/H-MFI Prepared by Solid-State Ion Exchange of $ZnCl_2$. *ACS Catal.* **2021**, *11* (23), 14489−14506.
(47) Zhai, H.; Bian, C.; Yu, Y.; Zhu, L.; Guo, L.; Wang, X.; Yu, Q.; Zhu, J.; Cao, X. Sustainable Route for Synthesis of All-Silica SOD Zeolite. *Crystals* **2019**, *9* (7), 338.

https://doi.org/10.1021/jacs.3c08484
J. Am. Chem. Soc. 2023, 145, 24191−24201